Nanoscale Advances

ROYAL SOCIETY OF CHEMISTRY

PAPER

View Article Online
View Journal | View Issue

Check for updates

Cite this: *Nanoscale Adv.*, 2025, 7, 124

Improved electrical and thermoelectric properties of electrodeposited $Bi_{1-x}Sb_x$ nanowire networks by thermal annealing†

Luc Piraux, *[a] Nicolas Marchal, [a] Pascal Van Velthem, [a] Tristan da Câmara Santa Clara Gomes, [a] Flavio Abreu Araujo, [a] Etienne Ferain, [ab] Jean-Paul Issi [a] and Vlad-Andrei Antohe *[ac]

Received 4th September 2024
Accepted 20th October 2024

DOI: 10.1039/d4na00735b

rsc.li/nanoscale-advances

Arrays of thermoelectric nanowires embedded in organic films are attracting increasing interest to fabricate flexible thermoelectric devices with adjustable dimensions and complex shapes, useful for sustainable power sources of portable electronic devices and wireless sensor networks. Here, we report the electrochemical synthesis of interconnected bismuth-antimony ($Bi_{1-x}Sb_x$) nanowires (with $0.06 < x < 0.15$) within the branched cylindrical nanopores of polycarbonate membranes. The influence of temperature and magnetic field on the electrical and thermoelectric properties was studied by considering electric and thermal currents flowing in the plane of the films. We show that short annealing times with temperature up to 250 °C of the nanowire-based nanocomposite lead to a large increase in the thermoelectric power, reaching values up to $-80\ \mu V\ K^{-1}$ at room temperature, which are comparable to those of bulk Bi-Sb alloys. In addition, we report Hall effect measurements on crossed nanowires, made possible for the first time by the remarkable electrical connectivity of the nanowire network. These measurements, combined with variations in temperature and under the magnetic field of the electrical resistance, indicate that the interconnected networks of $Bi_{1-x}Sb_x$ nanowires after thermal annealing behave like *n*-type, narrow band gap semiconductors. Overall, the electrical and thermoelectric properties near the ambient temperature of the heat-treated $Bi_{1-x}Sb_x$ nanowire networks are similar to those of bulk polycrystalline Bi-Sb alloys, which are well-known thermoelectric materials exhibiting optimal performance near and below room temperature.

1 Introduction

Bulk bismuth-antimony ($Bi_{1-x}Sb_x$) is a narrow-gap semiconductor for $0.06 < x < 0.2$, with attractive and optimal thermoelectric properties near and below ambient temperature.[1–3] At room temperature, polycrystalline $Bi_{1-x}Sb_x$ alloys exhibit a broad maximum of the figure of merit, *i.e.*, $ZT = S^2T/\rho\kappa \sim 0.3$ for $x \sim 0.12$,[4,5] where S, ρ and κ are the Seebeck coefficient (or thermopower), electrical resistivity and thermal conductivity, respectively, at temperature T. It has also been predicted theoretically that nanostructuring Bi-Sb alloys through the synthesis of nanowires (NWs), thin films and nanocomposites could lead to a higher ZT due to the quantum confinement effect.[6]

On the other hand, the development of lightweight and flexible thermoelectric materials[7,8] obtained by integrating thermoelectric NWs into organic hosts is attracting a great deal of interest because they are likely to harness the thermal energy of hot surfaces with complex geometries, or even of the human body, thus offering innovative prospects in the context of sustainable development and the powering of miniature, lightweight and functional portable electronic devices.[9–11] In this context, the electrochemical synthesis of three-dimensional (3D) networks of interconnected NWs in cross-pore polymer membranes a few tens of micrometers thick opens up new prospects in the field of flexible thermoelectricity, as recently demonstrated in the case of magnetic NWs.[8,12,13] Indeed, unlike parallel arrays of NWs where thermal and electric current can only be applied in the direction parallel to the axis of the NWs, *i.e.*, along the direction normal to the membrane film, the 3D NW structure allows also measurements to be made in the macroscopic direction of the film plane, taking advantage of the excellent electrical connectivity.[8,12,13] This unique architecture of crossed NWs (CNWs) embedded within organic polymer membranes not only makes it possible to considerably increase the thermoelectric output signal, but also to exploit the

---

[a] *Institute of Condensed Matter and Nanosciences (ICMN), Université catholique de Louvain (UCLouvain), Louvain-la-Neuve B-1348, Belgium. E-mail: luc.piraux@uclouvain.be*

[b] *it4ip s.a., Avenue Jean-Etienne Lenoir 1, Louvain-la-Neuve B-1348, Belgium*

[c] *R&D Center for Materials and Electronic & Optoelectronic Devices (MDEO), Faculty of Physics, University of Bucharest, Măgurele 077125, Ilfov, Romania. E-mail: vlad.antohe@fizica.unibuc.ro*

† Electronic supplementary information (ESI) available. See DOI: **https://doi.org/10.1039/d4na00735b**

advantages of transverse thermoelectricity, as recently demonstrated by Nernst measurements carried out on 3D arrays of pure Bi CNWs.[14] It is worth noting that interconnected arrays of thermoelectric nanomaterials have been synthesized by electrodeposition within 3D porous anodic alumina (AAO) templates.[15] However, although such 3D scaffolds including thermoelectric NWs can be produced on a large scale, the fragility of the inorganic AAO host makes this technology unsuitable for the preparation of flexible thermoelectric devices.

To date, little work has been done on the electrochemical synthesis of Bi-Sb alloy NWs[16–22] and even less on studying their thermoelectric properties.[21,22] For as-prepared Bi-Sb NWs, it appears that the Seebeck coefficients measured on parallel arrays of NWs[22] or single NWs[21] are significantly lower than those of bulk materials. In addition, the thermoelectric measurement performed on a single $Bi_{0.92}Sb_{0.08}$ NW after annealing at 180 °C under a nitrogen (N_2) atmosphere led to a slight reduction in the Seebeck coefficient.[21] In contrast, it was recently shown that both the resistivity and thermopower properties of 100 nm-thick Bi-Sb alloy films are enhanced with the overall microstructural quality, which improves with annealing temperature until close to the melting point.[23]

In this work, we report on the electrochemical synthesis and the effect of annealing on the electrical and thermoelectric properties of 230 nm diameter $Bi_{1-x}Sb_x$ alloy CNWs (with $0.06 < x < 0.15$) embedded in 3D porous polycarbonate (PC) membranes. Taking advantage of the interconnected structure of the NW network featuring an excellent electrical connectivity, Hall effect measurements were carried out for the first time on such a NW system, enabling the type and density of charge carriers to be determined. Such Hall effect measurements, which provide important information for electronic transport, are obviously not feasible to carry out on parallel NW arrays made by template-free or -assisted approaches. So far, previous Hall effect measurements have only been carried out on single InAs and InP semiconductor NWs grown by bottom-up techniques.[24–27] In this work, it was found that after short annealing times with temperature up to 250 °C, the $Bi_{1-x}Sb_x$ CNWs behave like *n*-type narrow-gap semiconductors and the Seebeck coefficients near room temperature, up to $-80\ \mu V\ K^{-1}$, are very close to those obtained in bulk polycrystalline Bi-Sb alloys and well above the thermopower values of Bi-Sb NWs reported to date.

2 Materials and methods

2.1 Sample preparation

In this work, 3D networks of CNWs made up of $Bi_{1-x}Sb_x$, where x is 0.06, 0.10 and 0.15, have been obtained through electrochemical deposition (ECD) within PC templates featuring interconnected cylindrical pores. Such 3D porous PC membranes with a thickness of 28 μm have been prepared by track-etching technology,[28] following a well-known procedure.[12,14,29–33] For this study, the PC films were subjected to a two-step irradiation process with heavy ions at angles of ±25° with respect to the normal to the surface, followed by a chemical dissolution of the latent tracks in a NaOH-based etchant. In this process, PC templates with an average pore diameter of 230 nm and an estimated porosity of about 20% were obtained. Subsequently, the as-prepared PC templates were covered onto one side by electron-beam evaporation (EBE), with a chromium (Cr, ∼15 nm)/copper (Cu, ∼2 μm) bi-layer to cover the nanopores and serve as a cathode during the subsequent Bi-Sb ECD process.

In a second step, $Bi_{1-x}Sb_x$ CNWs (x is 0.06, 0.10 and 0.15) were grown by ECD using a PAR 263A Potentiostat following a protocol slightly modified from that used for the growth of pure polycrystalline Bi CNWs.[14] In particular, $SbCl_3$ (antimony chloride) was added to an aqueous electrolyte commonly used for Bi growth and containing: 0.1 M $BiCl_3$ (bismuth chloride), 1 M HCl (hydrochloric acid fuming, 37%), 0.3 M $C_4H_6O_6$ (tartaric acid), 1 M NaCl (sodium chloride) and 1 M $C_3H_8O_3$ (glycerol). The different Sb content in the $Bi_{1-x}Sb_x$ deposit was adjusted by varying the $|Sb|/|Bi|$ molar ratio in the electrolyte to 0.4, 0.6 and 0.8, respectively. $Bi_{1-x}Sb_x$ CNWs were grown at room temperature by pulsed chronoamperometry in order to secure a uniform filling of the PC template. In this regard, −0.30 V was applied for 10 ms to electrochemically reduce the cations inside the pores close to the working electrode surface with a platinum (Pt) auxiliary electrode, followed by a potential of about −0.14 V for 90 ms to facilitate ion diffusion through the pores in the vicinity of the electrode between repetitive reduction steps. The latter potential value was always slightly adjusted to be close to the open circuit potential (OCP) of the cell to avoid electrochemical reduction during these relaxation periods. All the potentials were applied *versus* a silver/silver chloride (Ag/AgCl) reference electrode. Similar electrolyte compositions and electrochemical procedure were previously used to prepare $Bi_{1-x}Sb_x$ thin films,[34,35] as well as NWs or nanotubes (NTs) within AAO membranes.[19,20] For each of the samples prepared, the total duration of the ECD process was regulated by controlling the deposition charge, to ensure similar volumetric filling of the PC templates used. For the electrical measurements, the electrochemical growth of the NWs was restricted so that they did not emerge at the PC film surface and form macroscopic caps. For this series of samples, the porous membranes were partially filled and the thickness of the CNWs film was estimated to be 20 μm. Herewith, networks of CNWs made up of $Bi_{0.94}Sb_{0.06}$, $Bi_{0.90}Sb_{0.10}$ and $Bi_{0.85}Sb_{0.15}$, have been synthesized. The as-prepared samples were then rinsed with ultra-pure deionized water (DIW), dried out under a soft N_2 gas flow and kept under room ambient conditions until further manipulation.

The PC–$Bi_{1-x}Sb_x$ CNW nanocomposites were then subjected to a thermal annealing process at 250 °C under an N_2 atmosphere in a lab furnace, with a ramp rate of 10 °C min^{-1}. Once the maximum temperature was reached, the samples were cooled down to room temperature following approximately the same temperature ramp. It should be noted that the annealing temperature far exceeds the PC's glass transition temperature of about 150 °C. Under the usual conditions, this amorphous polymer softens gradually above this temperature and flows, which for the membranes used in this work leads to the rapid elimination of the porous structure. Interestingly, the 3D structure of the highly packed Bi-Sb CNW networks ensures the stability of the nanocomposites, whose mechanical properties are preserved. This is no longer the case if the annealing temperature reaches the melting temperature of $Bi_{1-x}Sb_x$ CNWs, which is very close to the melting point of Bi, *i.e.*, at 271.5 °C.[36] Also, as the annealing temperature is well below this point, no contamination of the $Bi_{1-x}Sb_x$ CNWs should occur due to the PC template.

2.2 Sample characterization

To perform electrical and thermoelectric measurements on $Bi_{1-x}Sb_x$ CNWs, the metal cathode was locally removed through a mechanical mask by galvanostatic electrochemical etching in a commercially available Cu electrolyte, at a current density of 0.5 A cm^{-2}, as described previously.[14] This fabrication process, followed by a simple scissor cut of the nanocomposite film, allows the geometry of the sample to be adapted to the experimental measurement concerned. While the parallel arrays of NWs traditionally studied in porous AAO or polymer membranes do not allow the Hall effect to be measured, it is worth pointing out that Hall measurements can be made in our system thanks to the branched NW structure. Fig. 1a and b show a drawing and a photograph, respectively, of a Hall bar arrangement used to combine measurements of electrical resistance and Hall effect. The current was directly injected into the rectangular Hall bar (about 2 cm long) from the unetched sections of the metallic cathode, where electrical contacts were made by Ag paint. The two contacts used to measure the Hall voltage are also seen in Fig. 1b. Typical resistance values of the prepared specimens were in the range of a few tens of ohms. Measurements of the electrical resistance, magnetoresistance and Hall effect of $Bi_{1-x}Sb_x$ CNWs with a diameter of 230 nm were carried out between 15 K and 300 K and up to a magnetic field of 0.8 T applied along the out-of-plane direction of the CNW films. Thermopower was measured between 110 K and 320 K under vacuum conditions using the set-up recently developed for pure Bi CNWs.[14] In this case, heat flow in the plane of the CNW film was generated by a resistive heater anchored on a Cu block at one end of the sample, the other end being in good thermal contact with a heat sink, as shown in Fig. 1c. The application of a temperature difference (ΔT) results in a thermoelectric voltage (ΔV). The voltage leads were made of thin chromel P wires and the temperature difference was measured with a small diameter type E differential thermocouple.

The morphological and elemental characterizations of the interconnected networks of $Bi_{1-x}Sb_x$ CNWs were performed using a JEOL 7600F field-emission scanning electron microscope (SEM) equipped with an energy-dispersive X-ray (EDX) detector. For this purpose, the PC templates were completely removed in dichloromethane and the self-supported CNW samples were afterwards placed on silicon (Si) wafers with the cathode-side facing downwards. The free-standing networks of CNWs were thick and dense enough to minimize the influence of the signals eventually emanating from the Si substrate and cathode layers during the local EDX spectroscopic analysis. Fig. 1d shows the SEM images of $Bi_{1-x}Sb_x$ CNWs with a diameter of 230 nm after the complete chemical dissolution of the polymer membrane. The CNW network exhibits the replicated

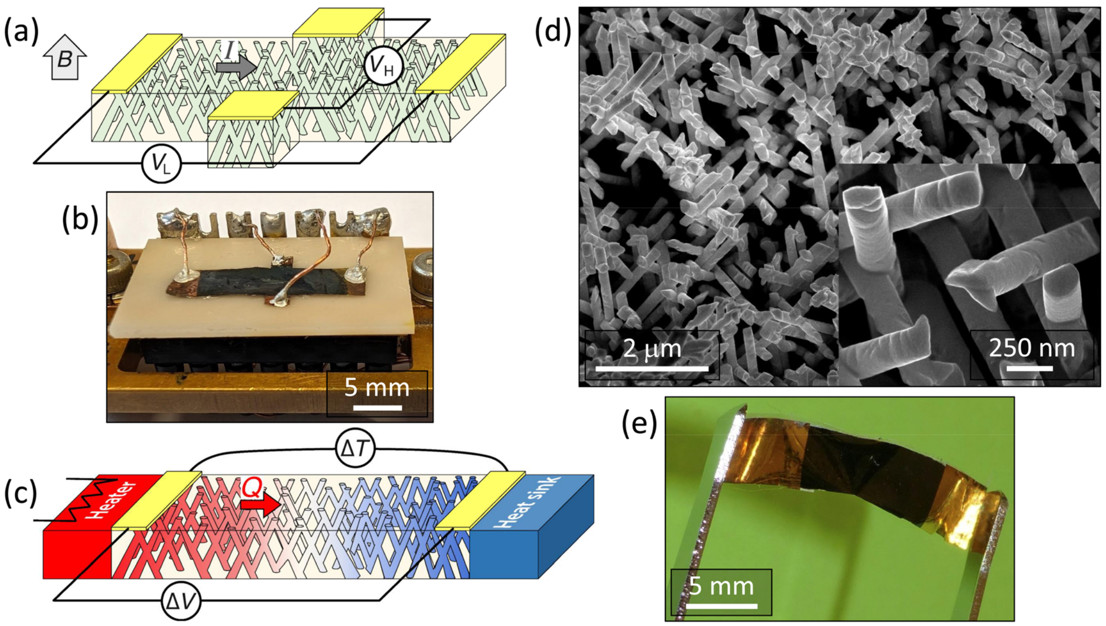

Fig. 1 (a and b) Schematic representation (a) and photograph (b) of the four-probe electrode design obtained by local etching of the cathode layers for measurements of the electrical resistance and Hall coefficient of the 3D networks of $Bi_{1-x}Sb_x$ CNWs. (c) Design of the experimental set-up for Seebeck coefficient measurements with the heat flow (Q) in the plane of the film made up of $Bi_{1-x}Sb_x$ CNWs. (d) Scanning electron microscope (SEM) images at two different magnifications showing the self-supported network of interconnected $Bi_{0.94}Sb_{0.06}$ CNWs, with the diameter of 230 nm and a 20% packing density. The SEM micrographs were taken after the complete dissolution of the polycarbonate (PC) template in dichloromethane. (e) Photograph of the flexible $Bi_{1-x}Sb_x$ CNW sample as-prepared for thermoelectric measurements.

complex branching morphology of the porous template and is mechanically robust and self-standing. The inset of Fig. 1d reveal the NW branched structure at higher magnification. Fig. 1e shows the PC-CNW nanocomposite film, highlighting the flexibility of the macroscopic sample and the ease of its handling.

In addition, the crystalline structure of the electrodeposited $Bi_{1-x}Sb_x$ CNWs was evaluated by X-ray diffraction (XRD) using a Bruker D8 Advance diffractometer equipped with a Lynxeye XE-T detector, operating with Cu K_α radiation ($\lambda = 1.54$ Å) at 1.2 kW. XRD data were acquired in a symmetric Bragg–Brentano geometry, in the range of $2\theta = 25°–70°$, with an angular step of 0.015° and an integration time of 0.15 s. For this purpose, the cathode layers from one side of the PC templates were completely removed by electrochemical etching as already explained, and subsequently the samples were carefully glued on a Si crystal sample holder. The EVA software package (Bruker) was employed for data acquisition and post-processing, whilst the AMCSD (American Mineralogist Crystal Structure Database) was used for phase identification. For displaying purpose, the Cu $K_{\alpha 2}$ contribution was stripped out and the amorphous background given by the PC templates was extracted from the XRD patterns.

3 Results and discussion

3.1 Elemental and structural investigation

Fig. 2a shows the EDX spectra of the $Bi_{1-x}Sb_x$ CNWs with different Sb content. As can be noticed, the EDX analysis indicates only the presence of the constitutive elements, *i.e.*, Bi and Sb, with no other contaminant traces present in the electrodeposited samples. In addition, the insets of Fig. 2a represent corresponding quantitative elemental calculation charts, demonstrating an Sb atomic percentage in the $Bi_{1-x}Sb_x$ alloy of approximately 6%, 10% and 15%, respectively, with increasing |Sb|/|Bi| molar ratios in the electrolyte during the CNW electrochemical growth.

Fig. 2b shows the XRD patterns of the various $Bi_{1-x}Sb_x$ CNWs obtained after an annealing process of the samples at 250 °C. For convenience, the AMCSD reference diffraction peaks data of Bi and Sb, both corresponding to the rhombohedral crystal system, are given at the bottom of the plots in blue and orange, respectively. As can be observed, the normalized XRD patterns include multiple peaks and all of them could be indexed to the same space group ($R\text{-}3m$) for all samples, with the most intense peak being reflected from the (012) planes of the trigonal unit cell. Clearly, the XRD data obtained confirm the polycrystalline nature of the $Bi_{1-x}Sb_x$ CNWs, with a weak preferential growth overall. It can also be noticed from Fig. 2b that the diffraction angle values (2θ) of all the identified peaks are between the expected positions for pure Bi and Sb, according to the AMCSD 0012839 and AMCSD 0009736 cards, respectively (see the reference patterns and 2θ values mentioned in Fig. 2b), indicating the formation of a Bi-Sb solid compound with no separated phase complexes. It can thus be concluded that Sb is progressively introduced within the Bi trigonal crystal system, causing its distortion that evolves with increasing the Sb content. Indeed, the ionic radius of Sb^{3+} (~2.06 Å) is smaller than that of Bi^{3+} (~2.30 Å).[37] In consequence, if Bi^{3+} ions are more and more substituted by Sb^{3+}, the lattice constant

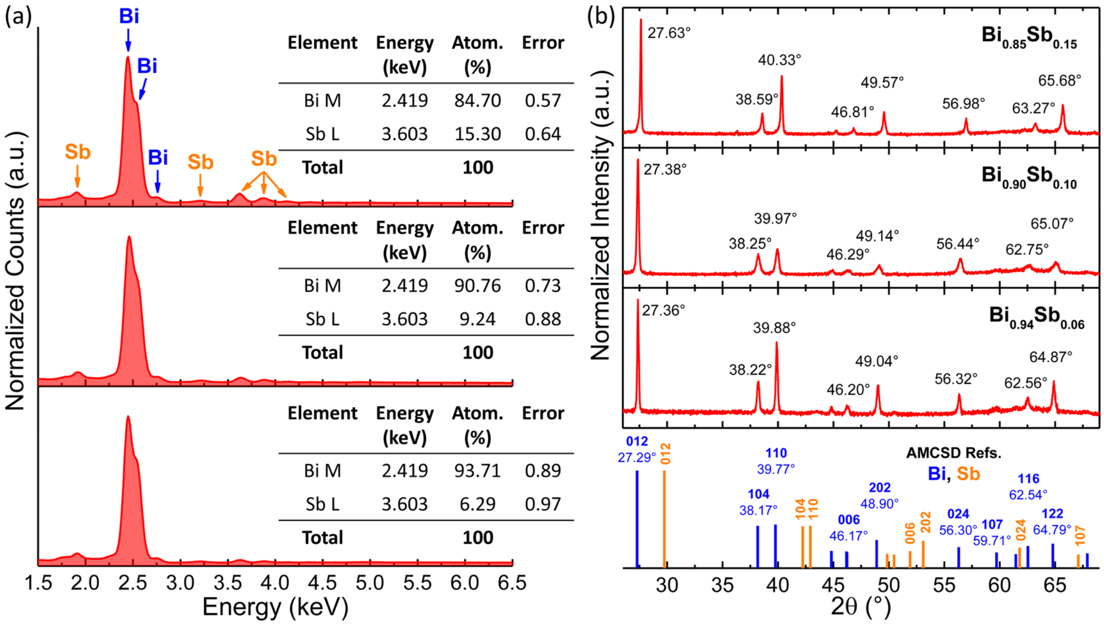

Element	Energy (keV)	Atom. (%)	Error
Bi M	2.419	84.70	0.57
Sb L	3.603	15.30	0.64
Total		100	

Element	Energy (keV)	Atom. (%)	Error
Bi M	2.419	90.76	0.73
Sb L	3.603	9.24	0.88
Total		100	

Element	Energy (keV)	Atom. (%)	Error
Bi M	2.419	93.71	0.89
Sb L	3.603	6.29	0.97
Total		100	

Fig. 2 (a) Energy dispersive X-ray (EDX) analysis of the 3D interconnected $Bi_{1-x}Sb_x$ CNWs, with approximately 6%, 10% and 15% atomic percentage of Sb, respectively. The spectra were obtained after complete dissolution of the PC templates in dichloromethane. The insets show corresponding quantitative compositional charts. (b) X-ray diffraction (XRD) patterns acquired on the various $Bi_{1-x}Sb_x$ CNWs embedded in PC templates. The data are normalized and the amorphous background given by the PC template was removed from the XRD patterns. Reference powder diffraction data of Bi (AMCSD 0012839) and Sb (AMCSD 0009736) are shown at the bottom in blue and orange, respectively.

decreases causing a progressive shift towards higher diffraction angles, as observed in all the acquired XRD patterns. Similar results were reported elsewhere, too, for electrodeposited Bi-Sb alloys of different elemental compositions.[19,34,35] It should be noted that a variation in the crystallite size of the $Bi_{1-x}Sb_x$ CNWs following the annealing step was not evidenced, as shown by the XRD patterns acquired on the as-deposited (not annealed) samples (see Fig. S1 in the ESI file†).

3.2 Electrical and thermoelectric measurements

The temperature dependence of the electrical resistance of the as-prepared and annealed $Bi_{1-x}Sb_x$ CNWs is shown in Fig. 3a and b, respectively. For all samples, the data have been normalized to the resistance value at room temperature. For the as-prepared samples, the variations of resistance between 15 K and 300 K are very small, showing a slight rise in resistance below room temperature followed by a small continuous decrease below $T = 175–225$ K. Noteworthily, the lower the Sb concentration, the more pronounced the decrease in electrical resistance at low temperature. Overall, the results of Fig. 3a are in good agreement with those previously reported for electrodeposited Bi-Sb NWs of comparable composition and diameter.[21,22]

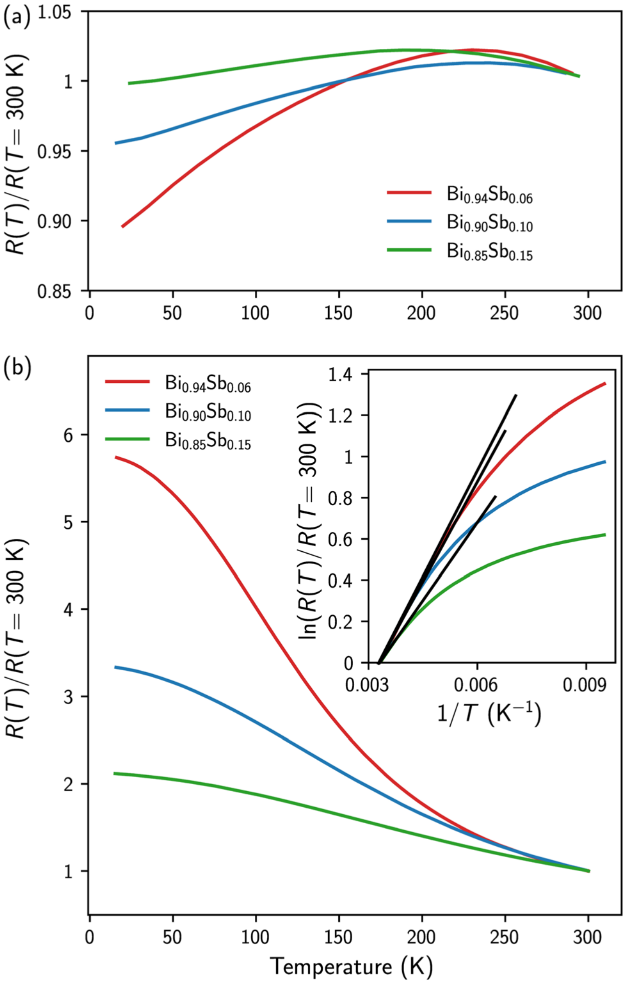

Fig. 3 (a and b) Temperature dependence of the electrical resistance of the as-prepared (a) and annealed (b) $Bi_{1-x}Sb_x$ CNWs. The data are normalized to values obtained at room temperature. The inset of (b) shows the variation of the logarithm of the normalized resistance *versus* the inverse of temperature for the annealed samples.

In contrast, the annealed $Bi_{1-x}Sb_x$ CNWs exhibit semiconducting behavior similar to that reported on bulk polycrystalline Bi-Sb alloys,[38–40] films prepared by evaporation,[41] and NWs made by introducing molten Bi-Sb alloys into the pores of AAO templates[42] and glass capillaries.[43] It should be emphasized that the temperature variation of the resistivity of narrow-gap semiconductors results from the opposing contributions of the charge carrier density, which increases monotonically with temperature and mobility, which in turn decreases with temperature due to the increase in electron–phonon collisions. While the temperature dependence of resistivity is dominated by electron mobility in Bi-Sb single crystals, giving rise to metallic behavior overall, semiconducting behavior is often observed in low-mobility polycrystalline materials (see the work of B. Lenoir *et al.*[2] and references therein). For $Bi_{1-x}Sb_x$ CNWs the temperature evolution of the electrical resistance reported in Fig. 3b shows that it is dominated by the temperature evolution of the carrier concentration. In the high temperature range, the electrical resistance of the samples exhibits semiconducting behavior with an exponential temperature dependence, *i.e.*, $R(T) \propto \exp(\varepsilon_g/2\,kT)$, with ε_g being the band gap.[44] Therefore, plotting the logarithm of the normalized resistance *versus* the inverse of temperature allows the evaluation of ε_g (see the inset of Fig. 3b). The band gap values thus obtained for the three $Bi_{1-x}Sb_x$ CNW samples ($\varepsilon_g = 58$ meV, 56 meV and 40 meV, for $x = 6\%$, 10% and 15%, respectively) agree with the values previously reported for nanostructured Bi-Sb alloys and thin films,[40,41,43,45,46] but they are 2–3 times larger than for bulk alloys.[2,4,44] Attempts have been made to explain these discrepancies by invoking confinement effects in nanometric-sized grains[47,48] and strain modified band structure.[45,46]

Hall effect measurements were performed at different temperatures between $T = 15$ K and $T = 300$ K, as shown in Fig. 4a–c. For all $Bi_{1-x}Sb_x$ CNWs, the variations in Hall resistance as a function of magnetic field show linear curves with negative slopes. This behavior indicates that conduction is dominated by electrons whose mobility is significantly higher than that of holes, in agreement with results obtained on bulk materials.[45,49,50] Fig. 4d shows the temperature variation of the electron carrier concentration (n) of $Bi_{1-x}Sb_x$ CNWs. The n values were estimated from the Hall resistance data in Fig. 4a–c, by considering the Bi-Sb alloys as one-type carrier systems. Therefore, the slopes of the Hall resistance *versus* magnetic field curves directly provide $1/ned$ where e is the electron charge and $d \sim 20$ μm is the thickness of the CNWs. Both the n values and temperature dependences shown in Fig. 4d are very similar to those previously reported for bulk Bi-Sb alloys and thin films,[45,49,50] reflecting the classical behavior of narrow-gap semiconductors. For $Bi_{1-x}Sb_x$ CNWs, a continuous increase in electron carrier concentration is observed with increasing Sb content in the alloy. At room temperature, n reaches values between 5 and 12 × 10^{18} cm^{-3} depending on the Sb

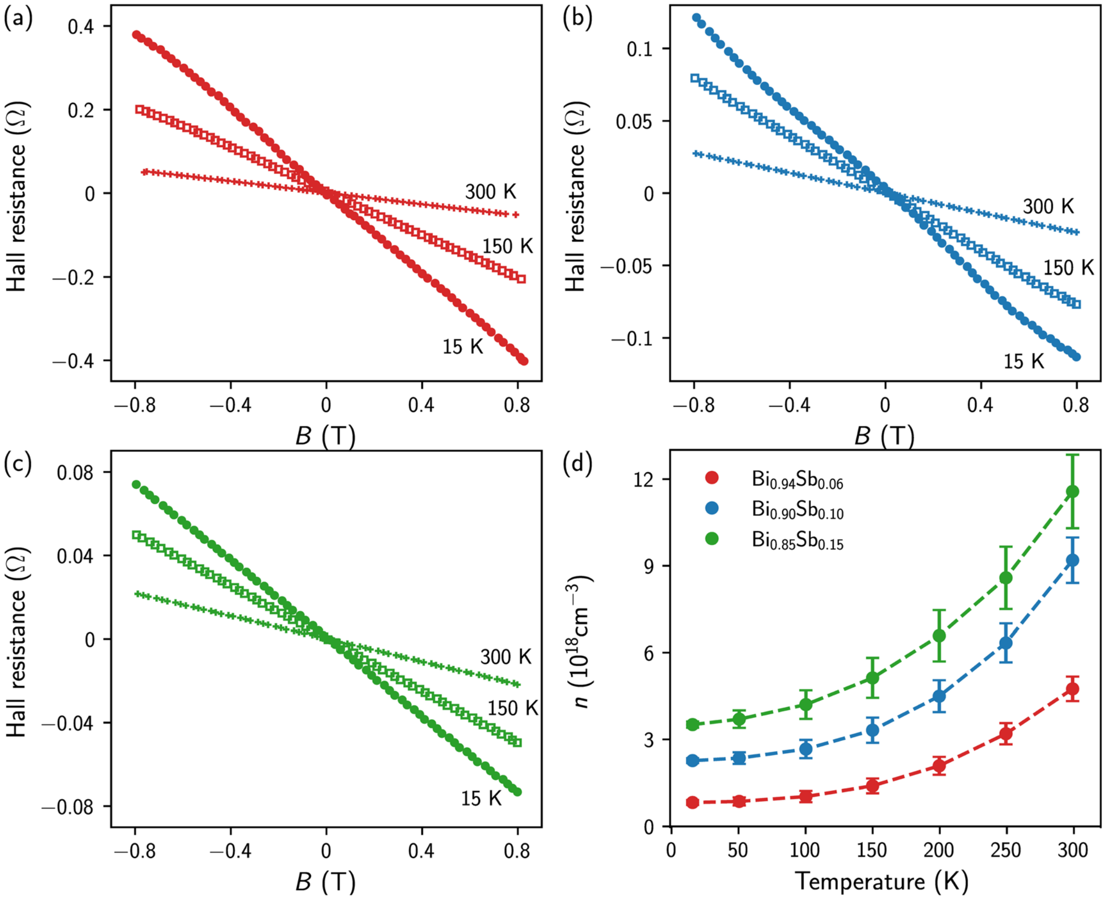

Fig. 4 (a–c) Magnetic field dependence of the Hall resistance of the annealed $Bi_{1-x}Sb_x$ CNWs at different temperatures for $x = 0.06$ (a), $x = 0.10$ (b) and $x = 0.15$ (c). (d) Temperature dependence of the carrier concentration of the annealed $Bi_{1-x}Sb_x$ CNWs.

concentration. Values of n lowered by a factor of 4 to 7 are obtained at $T = 15$ K.

Low-field magnetoresistance measurements ($B \leq 0.8$ T) were carried out on these same samples at identical temperatures, as shown in Fig. 5a–c. The magnetoresistance, *i.e.*, $\mathrm{MR} = 100 \times [R(B) - R(B = 0)]/R(B = 0)$, is expressed in %. All $Bi_{1-x}Sb_x$ CNWs show a quadratic variation of MR with magnetic field, due to the classical Lorentz force contribution to the charge carrier scattering. By fitting the experimental data to the $\mathrm{MR} = AB^2$ law, the A coefficient was extracted for the various $Bi_{1-x}Sb_x$ CNWs at different temperatures, as shown in Fig. 5d. Since the units of the A coefficient at T^{-2} are those of the square of the electron mobility, the decrease in A with increasing Sb concentration is due to the increased impurity scattering. For the $Bi_{1-x}Sb_x$ CNWs, the decrease in electron mobility above $T = 100$ K results from collisions between electrons and phonons. For $T < 100$ K, A varies little with temperature, indicating dominant electron scattering by impurities and static defects. For polycrystalline Bi-Sb alloys, it has been shown that grain size decreases with Sb concentration.[39] This could explain the evolution of the A coefficient with Sb concentration shown in Fig. 5d. As the relative decreases in the square root of A between $T = 15$ K and $T = 300$ K (between 1.8 and 2.2, depending on the alloy composition) are significantly smaller than the increases in charge carrier concentration over the same temperature range (see Fig. 4d), the electrical resistance of $Bi_{1-x}Sb_x$ CNWs exhibits the overall semiconductor behavior shown in Fig. 3b.

The temperature variation of the thermoelectric power between 110 K and 320 K of the as-prepared and annealed $Bi_{1-x}Sb_x$ CNWs is shown in Fig. 6. For comparison, previously measured values of the thermopower of a pure Bi CNW sample with the same wire diameter of 230 nm are also reported in the temperature range investigated (the dashed line in Fig. 6).[14] For all samples, the thermoelectric power is negative, due to the higher mobilities of electrons compared to those of holes. The thermopower of the as-prepared samples decreases progressively with the Sb concentration in the alloy, from −70 μV K^{-1} for $Bi_{0.94}Sb_{0.06}$ to −28 μV K^{-1} for $Bi_{0.85}Sb_{0.15}$ at room temperature. Annealing leads to a sharp rise in the absolute values of the thermopower over the entire temperature range. At room temperature, the absolute values of the thermopower of the annealed $Bi_{0.90}Sb_{0.10}$ and $Bi_{0.85}Sb_{0.15}$ CNWs are approximately twice as high as the values for the as-prepared samples, while the increase in the Seebeck coefficient is significantly less for $Bi_{0.94}Sb_{0.06}$ CNWs. For $Bi_{0.94}Sb_{0.06}$ and $Bi_{0.90}Sb_{0.10}$ CNWs, the thermopower reaches −80 μV K^{-1} at room temperature, which is much higher than the thermopower of pure Bi CNWs (see Fig. 6) and bulk polycrystalline Bi,[51–53] close to −60 μV K^{-1}. It is

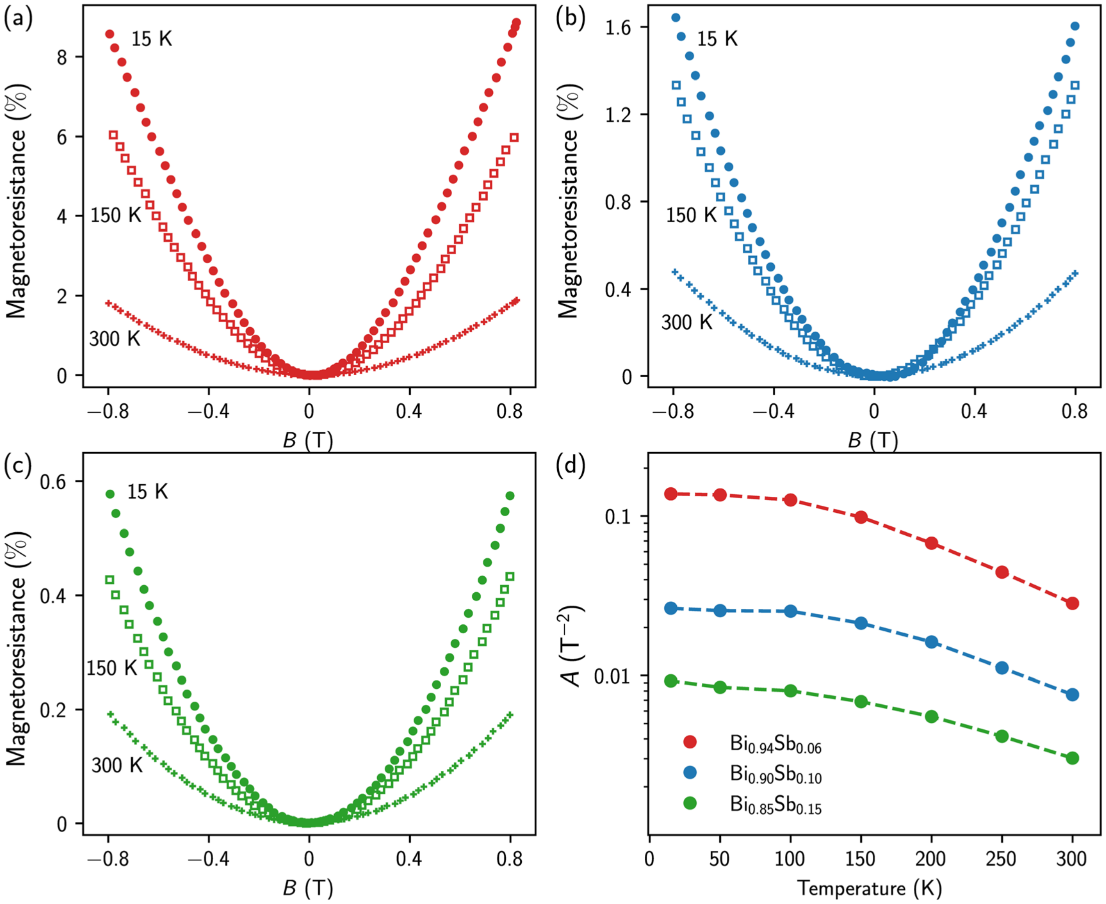

Fig. 5 (a–c) Magnetoresistance of annealed $Bi_{1-x}Sb_x$ CNWs at different temperatures for $x = 0.06$ (a), $x = 0.10$ (b) and $x = 0.15$ (c). (d) Temperature dependence of the amplitude of the magnetoresistance coefficient (A), fitted in a range of ±0.8 T.

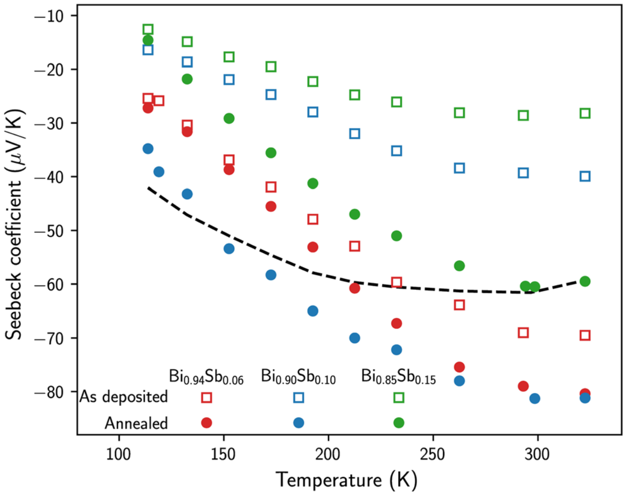

Fig. 6 Temperature dependence of the Seebeck coefficient of the as-prepared and annealed $Bi_{1-x}Sb_x$ CNWs. The dashed line shows the data obtained on a pure Bi CNW sample with the same diameter of 230 nm.[14]

stressed that the thermopower values in Fig. 6 obtained for annealed $Bi_{1-x}Sb_x$ CNWs are much higher than those reported to date for Bi-Sb NWs prepared by ECD[21,22] and by injecting the molten alloy into the pores of AAO templates.[42] Indeed, the room-temperature thermopower of single electrodeposited $Bi_{0.90}Sb_{0.10}$ NWs with a diameter of 220 nm reached -52 μV K^{-1} for the as-prepared samples and -45 μV K^{-1} for the annealed wires at 180 °C for 15 h.[21] Also, previous measurements performed on parallel arrays of $Bi_{1-x}Sb_x$ NWs synthesized by ECD in polymer membranes with a diameter of 80 nm and $0.1 < x < 0.33$ showed a continuous decrease in thermopower with increasing Sb concentration and values between -32 μV K^{-1} ($x = 0.1$) and -8 μV K^{-1} ($x = 0.33$) at room temperature.[22] In addition, the Seebeck coefficient at $T = 300$ K for Bi-Sb NW arrays made by melt injection in AAO was found to be between -50 μV K^{-1} and -60 μV K^{-1}.[42] The observed improvement in the electrical and thermoelectric properties of the $Bi_{1-x}Sb_x$ CNWs following annealing can be attributed to a more homogeneous distribution of Sb atoms in the NWs. It is also interesting to note that the thermopower values obtained at room temperature on annealed $Bi_{1-x}Sb_x$ CNWs are very close to those of bulk alloys and thin films prepared by evaporation, *i.e.*, around -90 μV K^{-1}.[2,38,41,45,49,54] However, there are marked differences in the temperature dependence of thermopower when the samples are cooled to low temperatures. For bulk and thin film Bi-Sb alloys, the thermopower increases significantly up to $T = 50$–200 K, reaching values as high as -120 μV K^{-1}, before decreasing at lower temperatures.[2,38,41,45,49,50,54] In contrast, the thermopower of annealed $Bi_{1-x}Sb_x$ CNWs decreases continuously with cooling below $T = 300$ K (see Fig. 6). A very similar behavior of the temperature dependence of the thermopower has been reported for Bi-Sb NW composites made using a wet-chemical method.[50]

4 Conclusions

In this work, we report on the synthesis and characterization of interconnected NW networks of $Bi_{1-x}Sb_x$ alloys of controlled composition ($0.06 < x < 0.15$) obtained by ECD in 3D porous PC membranes. We demonstrated that short annealing times with temperature up to 250 °C of the PC-$Bi_{1-x}Sb_x$ nanocomposite film considerably improve its electrical and thermoelectric properties while preserving the physical integrity of the nanocomposite film thanks to the highly-packed NW networks. For all $Bi_{1-x}Sb_x$ CNWs, the Seebeck coefficient after annealing increases sharply compared with the values measured on the as-prepared samples, reaching values of $-80\ \mu V\ K^{-1}$ for $Bi_{0.94}Sb_{0.06}$ and $Bi_{0.90}Sb_{0.10}$ CNWs, close to those obtained in bulk materials and well above the thermopower values of Bi-Sb NWs reported to date. The temperature dependence of the thermopower, measured between $T = 320$ K and $T = 10$ K, shows a broad plateau near room temperature followed by a gradual decrease at lower temperatures. In addition, we also report for the first time Hall effect measurements on interconnected NW networks, made possible by the remarkable electrical connectivity within the Bi-Sb NWs. The charge carrier densities and their temperature evolution extracted from Hall effect measurements agree with previously reported data for bulk Bi-Sb alloys and thin films. Overall, the electrical measurements as a function of temperature and magnetic field carried out on $Bi_{1-x}Sb_x$ CNWs are consistent with the behavior of an *n*-type narrow-gap semiconductor. Finally, the possibility of making transverse magneto-transport measurements in these interconnected NW network films also offers new prospects for applications in the field of flexible sensors and flexible transverse thermoelectric devices based on the Nernst effect, as recently shown for pure Bi CNWs.[14]

Data availability

Data supporting this study are openly available from Zenodo at **https://doi.org/10.5281/zenodo.12581490**.

Author contributions

Luc Piraux: conceptualization, formal analysis, funding acquisition, investigation, methodology, project administration, resources, supervision, validation, visualization, writing – original draft, writing – review & editing; Nicolas Marchal: data curation, formal analysis, investigation, visualization; Pascal Van Velthem: formal analysis, investigation, methodology; Tristan da Câmara Santa Clara Gomes: data curation, formal analysis, investigation, visualization; Flavio Abreu Araujo: data curation, formal analysis, investigation, visualization; Etienne Ferain: investigation, resources, visualization; Jean-Paul Issi: formal analysis, investigation, visualization, writing – review & editing; Vlad-Andrei Antohe: data curation, formal analysis, investigation, methodology, validation, visualization, writing – original draft, writing – review & editing. All authors have read and agreed to the published version of the manuscript.

Conflicts of interest

There are no conflicts to declare.

Acknowledgements

Financial support was provided by the Belgian Fund for Scientific Research (F.R.S.-FNRS). F. A. A. receives support as a Research Associate of the F.R.S.-FNRS. Authors would like to thank François Devred for his help with the XRD measurements.

References

1 G. S. Nolas, J. Sharp and H. J. Goldsmid, *Thermoelectrics. Basic Principles and New Materials Developments*, Springer, Springer-Verlag, Berlin, Heidelberg, 1st edn, 2001, p. 293.
2 B. Lenoir, H. Scherrer and T. Caillat, in *Recent Trends in Thermoelectric Materials Research I*, ed. T. M. Tritt, Elsevier, 2001, vol. 69, pp. 101–137.
3 J. P. Heremans and H. Jin, *Optical and Electronic Cooling of Solids*, 2016, p. 976507.
4 B. Lenoir, M. Cassart, J. P. Michenaud, H. Scherrer and S. Scherrer, *J. Phys. Chem. Solids*, 1996, **57**, 89–99.
5 H. Jin and J. P. Heremans, *Phys. Rev. Mater.*, 2018, **2**, 115401.
6 S. Tang and M. S. Dresselhaus, *J. Mater. Chem. C*, 2014, **2**, 4710–4726.
7 Y. Chen, M. He, B. Liu, G. C. Bazan, J. Zhou and Z. Liang, *Adv. Mater.*, 2017, **29**, 1604752.
8 T. da Câmara Santa Clara Gomes, N. Marchal, F. A. Araujo and L. Piraux, *J. Phys. D: Appl. Phys.*, 2022, **55**, 223001.
9 Z. Fan, Y. Zhang, L. Pan, J. Ouyang and Q. Zhang, *Renewable Sustainable Energy Rev.*, 2021, **137**, 110448.
10 Y. Wang, L. Yang, X. L. Shi, Z. Shi, L. Chen, M. S. Dargusch, J. Zou and Z. G. Chen, *Adv. Mater.*, 2019, **31**, 1807916.
11 L. Zhang, X. L. Shi, Y. L. Yang and Z. G. Chen, *Mater. Today*, 2021, **46**, 62–108.
12 T. da Câmara Santa Clara Gomes, F. A. Araujo and L. Piraux, *Sci. Adv.*, 2019, **5**, eaav2782.
13 F. A. Araujo, T. da Câmara Santa Clara Gomes and L. Piraux, *Adv. Electron. Mater.*, 2019, **5**, 1800819.
14 L. Piraux, N. Marchal, P. V. Velthem, T. da Câmara Santa Clara Gomes, E. Ferain, J. P. Issi and V. A. Antohe, *Nanoscale*, 2023, **15**, 13708–13717.
15 A. Ruiz-Clavijo, O. Caballero-Calero, C. V. Manzano, X. Maeder, A. Beardo, X. Cartoixà, F. X. Álvarez and M. Martín-González, *ACS Appl. Energy Mater.*, 2021, **4**, 13556–13566.

16 A. L. Prieto, M. Martín-González, J. Keyani, R. Gronsky, T. Sands and A. M. Stacy, *J. Am. Chem. Soc.*, 2003, **125**, 2388–2389.

17 L. Li, G. Li, Y. Zhang, Y. Yang and L. Zhang, *J. Phys. Chem. B*, 2004, **108**, 19380–19383.

18 X. Dou, Y. Zhu, X. Huang, L. Li and G. Li, *J. Phys. Chem. B*, 2006, **110**, 21572–21575.

19 X. Dou, G. Li, X. Huang and L. Li, *Nanoscale Res. Lett.*, 2010, **5**, 1118–1123.

20 X. Dou, G. Li, X. Huang and L. Li, *J. Phys. Chem. C*, 2008, **112**, 8167–8171.

21 S. Heiderich, W. Toellner, T. Boehnert, J. G. Gluschke, S. Zastrow, C. Schumacher, E. Pippel and K. Nielsch, *Phys. Status Solidi RRL*, 2013, **7**, 898–902.

22 M. Cassinelli, S. Müller, K. O. Voss, C. Trautmann, F. Völklein, J. Gooth, K. Nielsch and M. E. Toimil-Molares, *Nanoscale*, 2017, **9**, 3169–3179.

23 M. P. Siegal, A. L. Lima-Sharma, P. A. Sharma and C. Rochford, *Appl. Phys. Lett.*, 2017, **110**, 141905.

24 K. Storm, F. Halvardsson, M. Heurlin, D. Lindgren, A. Gustafsson, P. M. Wu, B. Monemar and L. Samuelson, *Nat. Nanotechnol.*, 2012, **7**, 718–722.

25 C. Blömers, T. Grap, M. I. Lepsa, J. Moers, S. Trellenkamp, D. Grützmacher, H. Lüth and T. Schäpers, *Appl. Phys. Lett.*, 2012, **101**, 152106.

26 O. Hultin, G. Otnes, M. T. Borgström, M. Björk, L. Samuelson and K. Storm, *Nano Lett.*, 2016, **16**, 205–211.

27 O. Hultin, G. Otnes, L. Samuelson and K. Storm, *Nano Lett.*, 2017, **17**, 1121–1126.

28 E. Ferain and R. Legras, *Nucl. Instrum. Methods Phys. Res., Sect. B*, 2003, **208**, 115–122.

29 L. Piraux, V. A. Antohe, E. Ferain and D. Lahem, *RSC Adv.*, 2016, **6**, 21808–21813.

30 J. O. Omale, P. V. Velthem, V. A. Antohe, A. Vlad and L. Piraux, *Energy Technol.*, 2021, **9**, 2100062.

31 J. O. Omale, R. Rupp, P. V. Velthem, V. V. Kerckhoven, V. A. Antohe, A. Vlad and L. Piraux, *Energy Storage Mater.*, 2019, **21**, 77–84.

32 A. Vlad, V. A. Antohe, J. M. Martínez-Huerta, E. Ferain, J. F. Gohy and L. Piraux, *J. Mater. Chem. A*, 2016, **4**, 1603–1607.

33 E. Araujo, A. Encinas, Y. Velázquez-Galván, J. M. Martínez-Huerta, G. Hamoir, E. Ferain and L. Piraux, *Nanoscale*, 2015, **7**, 1485–1490.

34 F. Besse, C. Boulanger, B. Bolle and J. J. Heizmann, *Scr. Mater.*, 2006, **54**, 1111–1115.

35 P. M. Vereecken, S. Ren, L. Sun and P. C. Searson, *J. Electrochem. Soc.*, 2003, **150**, C131.

36 C. Rochford, D. L. Medlin, K. J. Erickson and M. P. Siegal, *APL Mater.*, 2015, **3**, 126106.

37 S. S. Batsanov, *Inorg. Mater.*, 2001, **37**, 871–885.

38 R. Martin-Lopez, A. Dauscher, H. Scherrer, J. Hejtmanek, H. Kenzari and B. Lenoir, *Appl. Phys. A: Mater. Sci. Process.*, 1999, **68**, 597–602.

39 K. Malik, D. Das, D. Mondal, D. Chattopadhyay, A. K. Deb, S. Bandyopadhyay and A. Banerjee, *J. Appl. Phys.*, 2012, **112**, 083706.

40 C. H. Will, M. T. Elm, P. J. Klar, B. Landschreiber, E. Güneş and S. Schlecht, *J. Appl. Phys.*, 2013, **114**, 193707.

41 E. Osmic, J. Barzola-Quiquia, W. Böhlmann, P. G. Bercoff, L. Venosta and P. Häussler, *J. Phys. Chem. Solids*, 2022, **167**, 110734.

42 Y. M. Lin, O. Rabin, S. B. Cronin, J. Y. Ying and M. S. Dresselhaus, *Appl. Phys. Lett.*, 2002, **81**, 2403–2405.

43 l. A. Konopko, A. A. Nikolaeva, T. E. Huber and J. P. Ansermet, *J. Low Temp. Phys.*, 2016, **185**, 673–679.

44 A. L. Jain, *Phys. Rev.*, 1959, **114**, 1518–1528.

45 S. Cho, A. DiVenere, G. K. Wong, J. B. Ketterson and J. R. Meyer, *J. Appl. Phys.*, 1999, **85**, 3655–3660.

46 S. Cho, A. DiVenere, G. K. Wong, J. B. Ketterson and J. R. Meyer, *Phys. Rev. B: Condens. Matter Mater. Phys.*, 1999, **59**, 10691–10696.

47 O. Rabina, Y. M. Lin and M. S. Dresselhaus, *Appl. Phys. Lett.*, 2001, **79**, 81–83.

48 S. Tang and M. S. Dresselhaus, *Phys. Rev. B: Condens. Matter Mater. Phys.*, 2012, **86**, 075436.

49 H. Kitagawa, H. Noguchi, T. Kiyabu, M. Itoh and Y. Noda, *J. Phys. Chem. Solids*, 2004, **65**, 1223–1227.

50 K. Vandaele, B. He, P. V. D. Voort, K. D. Buysser and J. P. Heremans, *Phys. Rev. Appl.*, 2018, **9**, 024020.

51 J. P. Issi, in *Thermoelectrics Handbook: Macro to Nano*, ed. D. M. Rowe, CRC Press, Taylor & Francis Group, 6000 Broken Sound Parkway NW, Suite 300, Boca Raton, FL 33487-2742, 1st edn, 2006, ch. 30, pp. 1–12.

52 Y. Hasegawa, M. Murata, D. Nakamura, T. Komine, T. Taguchi and S. Nakamura, *J. Appl. Phys.*, 2009, **105**, 103715.

53 T. Arisaka, M. Otsuka, M. Tokitani and Y. Hasegawa, *J. Appl. Phys.*, 2019, **126**, 085101.

54 I. Vurgaftman, J. R. Meyer, C. A. Hoffman, S. Cho, A. DiVenere, G. K. Wong and J. B. Ketterson, *J. Phys.: Condens. Matter*, 1999, **11**, 5157.